J Mater Sci: Mater Electron (2020) 31:21248–21259

Investigation of physical properties of Fe_2O_3 and graphene-based sandwich-type electrodes for biosensor technology

C. Gökhan Ünlü[1,*]

[1] *Department of Biomedical Engineering, Pamukkale University, 20070 Denizli, Turkey*

Received: 29 July 2020
Accepted: 8 October 2020
Published online: 19 October 2020

ABSTRACT

The usage of composite materials in which graphene combined with magnetic nanoparticles offers benefits for biomedical applications. Stabilization of nanoparticles on the electrode surface which is necessary for biosensors and other applications is still an important issue to be solved. Here the stabilization of the nanoparticles is achieved by inserting nanoparticles between two graphene layers in a sandwich structure. Furthermore, it has been theoretically predicted that sandwich-type structures prepared with metal nanoparticles between two graphene layers would have extraordinary physical properties. In this study, Fe_2O_3/SLG (single-layer graphene) and the sandwich-type SLG/Fe_2O_3/SLG electrodes were produced. Fe_2O_3 nanoparticles were synthesized by the sol–gel method, and graphene was produced by CVD (chemical vapor deposition) on Cu foil and then transferred onto FTO (fluorine-doped tin oxide). Fe_2O_3/SLG composite structure was produced by the drop-casting process. The structural, magnetic, and electrochemical properties of samples were investigated in detail. Structural analysis revealed that Fe_2O_3 has an α-phase with a rhombohedral crystal structure and the mean particle diameter is 128 nm. Raman and SEM analysis also confirmed the quality of SLG and the sandwich-type graphene structure. The nanoparticles have a magnetic phase transition which has Morin temperature at about T = 263 K. Also, Fe_2O_3 nanoparticles have shown ferromagnetic behavior at room temperature with 0.16 Am^2/kg remanent magnetization and 0.203 T coercive field. This work demonstrates the effectiveness of graphene sandwich-type electrodes to eliminate the main stabilization obstacle of magnetic nanoparticles especially for biosensor applications.

Address correspondence to E-mail: cunlu@pau.edu.tr

https://doi.org/10.1007/s10854-020-04637-4

1 Introduction

Recently, graphene, a single layer of carbon atoms, is one of the most crucial technological developments owing to its extraordinary physical properties. The relatively small bond length (0.0142 nm) makes graphene tougher than the steel and extremely flexible material as well. Recently its low resistivity (10^{-8} Wm) and transparency makes graphene a promising material for the electronic industry, energy storage, medicine, and biosensor technology [1–4]. Furthermore it makes an effective interface between enzyme and electrode, allowing the improvement of biosensors in terms of high sensitivity and short current response time [5, 6]. So far many methods have been proposed to produce graphene among which the Hummers method is the foremost commonly used [7–13]. However, the graphene oxide (GO) and reduced GO flakes obtained by this method are generally in the order of micrometers. Alternatively, graphene can be directly transformed from amorphous carbides by chlorination under low temperatures and ambient pressures [14–16]. Among them, the most promising technique is the CVD technique to get high-quality, uniformity and large-scale (the order of cm) graphene [17, 18].

Nowadays graphene composites containing magnetic nanoparticles (MNPs) such as transition metals and their oxides are attracting great attention owing to their magnetic properties that are useful for medicine and biosensor applications [19–45]. Therefore graphene gains new functionality with the MNPs. The unique properties and production methods of these graphene-based composites are still under investigation and new and green synthesis approaches are challenging. Up to now Fe-based metal oxide nanoparticles, magnetite (Fe_3O_4), maghemite (γ-Fe_2O_3) and hematite (α-Fe_2O_3) have been used as contrast agents in magnetic resonance imaging, drug carriers, as well as inducers for hyperthermia of tumors [46–49]. Among them, hematite is widely studied because it is the most stable iron oxide with high resistance to corrosion, not expensive, easy to find, biocompatible, environmentally friendly and non-toxic [50–54]. Especially, hematite is the most promising modifying material because of the variable valence state of iron oxides that can be recovered in situ via electrochemical reducing or oxidizing during the sensing process [50].

The nanosized 3d elements (Co, Ni, Fe) and their oxides have been mostly decorated on the graphene layer because their redox states, and electrochemical stabilities [55] play an essential role to produce for glucose detection [7], and MNPs can easily connect with the glucose enzyme. Fe_3O_4/GO has been presented to be both glucose and H_2O_2 sensor [8]. Furthermore, Li et al. [9] reported Fe_2O_3/graphene systems show better results for the lithium storage battery. In another study, α-Fe_2O_3 NPs with various morphologies were synthesized and the electrocatalytic activities of dopamine (DA) and uric acid (UA) at Fe_2O_3/GO nanohybrids decorated glassy carbon electrodes were measured by Cai et al. [13]. In the study, the electrochemical measurements exhibited that the discal Fe_2O_3 NPs had the most remarkable electrochemical response toward the simultaneous detection of DA and UA.

Graphene can be decorated with nanoparticles (magnetic or non-magnetic) using different techniques such as the chemical, the electrochemical, the sputtering, etc. Selection of the decorated nanoparticle depends on the interaction between the nanoparticle and enzyme and, at the same time, degradation of the nanoparticle (cycle, photo, chemical, etc.) has a significant effect since measurement cycles cause the degradation, and removal of the nanoparticle or nanoparticles from the graphene surface decreases the sensitivity of the biosensor. Furthermore, graphene which is decorated with nanoparticle systems have been developed as well [10, 11]. In 2016, Feng et al. worked on multilayered Fe_2O_3/graphene where graphene oxide layers were prepared with a modified Hummers method [12]. This structure exhibits superior catalytic activity toward the oxygen evolution reaction for Li batteries. Moreover sandwich-type graphene, two slices of single-layer graphene with encapsulated nanoparticles is shown theoretically as a super-strong, conductive material enhancing desired electronic and optical properties. When binding molecules between nanoparticles and graphene are not used, nanoparticles are placed using Van der Waals forces on the SLG. Therefore, nanoparticles in biosensor applications are challenging in terms of stability. Sandwich-type graphene is proposed to overcome this issue [56]. The numbers of nanoparticles are limited by the graphene layers which significantly improved the sensitivity of the system for biosensor applications

due to stability in the number of nanoparticles between layers.

In this study, Fe_2O_3/SLG and sandwich-type SLG/Fe_2O_3/SLG composites were prepared on FTO by CVD, drop-casting and sol–gel methods. Fe_2O_3 nanoparticles were fabricated by the sol–gel method and the CVD method was used to produce graphene. The structural characterizations were done by the X-ray diffraction (XRD), Raman spectroscopy, Energy Dispersive X-ray (EDX), X-ray photoelectron spectroscopy (XPS), optical microscopy and scanning electron microscopy (SEM). Magnetic properties of the nanomaterials were analyzed using a vibrating sample magnetometer (VSM) option of Quantum Design PPMS. In addition, the electrochemical analyses were carried out in a cell with three electrodes.

2 Experimental

2.1 Graphene growth

Single-layer graphene (SLG) was produced by using CVD technique. 0.1 mm thick, 2 × 2 cm^2 Cu foils of 99.8% purity was used as a metallic catalyzer. Copper foils were pre-cleaned by acetone, isopropanol, and deionized water for 10 min in an ultrasonic cleaner. Then, it was placed in a furnace. The furnace was evacuated to 10^{-6} Torr and pre-heated to 1000 °C with flowing H_2 at 100 sccm for 30 min. This pre-heating and annealing process for Cu is targeted to create graphene seeds for growth. After annealing, CH_4 gas was let into the chamber at 30 sccm flow for 30 min. The chamber pressure was kept at 9 × 10^2 Torr while holding the Cu substrate at 1000 °C during the growth of the graphene film. Finally, the Cu foil covered with graphene was quickly cooled to room temperature.

2.2 Transfer procedure of graphene to FTO substrates

The large-area SLG graphene prepared on the Cu foils was transferred onto FTO substrates. To be able to carry out the transfer, graphene on Cu foil was covered homogeneously with PMMA (Polymethyl methacrylate) solution with a spin-coater rotating at 4000 rpm for 40 s. Then, the sample was floated onto $Fe(NO_3)_3$*$9H_2O$ for a day in order to have the Cu substrate etched. The remaining graphene with PMMA was transferred onto the FTO substrate by the fishing process. Then the PMMA solution was removed by acetone.

2.3 Synthesis of Fe_2O_3 nanoparticles

Fe_2O_3 was prepared by the sol–gel technique. Appropriate amount of $Fe(NO_3)_3$*$9H_2O$ was dissolved in water in order to obtain desired stoichiometry. Afterward, citric acid and ethylene glycol were added to the mixture. A viscous residue was formed by slowly boiling this solution at 200 °C. The obtained residue was dried at 300 °C until a dry-gel was formed. Finally, the residual precursor was burned in the air at 600 °C for 12 h in order to remove the organic materials produced in the chemical reactions, and the remaining powder material was grounded in a mortar to obtain homogenous materials.

2.4 Production of Fe_2O_3/SLG and sandwich-type SLG/Fe_2O_3/SLG electrode

Nanoparticles produced by the sol–gel method were dissolved in ethanol for 10 min through an ultrasonic cleaner and then the solution was left for 30 min for large particles to collapse. The nanoparticle solution was taken from near the surface by pipet and the solution was dropped onto SLG/FTO by drop-casting and dried under room conditions to produce Fe_2O_3/SLG composite. Also, the production of sandwich-type SLG/ Fe_2O_3/SLG had followed the same procedure with Fe_2O_3 on graphene, and then, another single-layer graphene sheet was transferred on Fe_2O_3/SLG.

2.5 Characterizations

X-ray diffraction (XRD) was used for the structural analysis of Fe_2O_3 nanoparticles. XRD patterns were collected at room temperature using Cu-K_α radiation. FullProf software was used for data processing [6]. Raman spectroscopy was used for analyses of graphene properties. The morphology analyses were performed by SEM (Ziess/Supra 55 FE-SEM) and optical microscopy (Optica B-1000MET). EDX and XPS analyses were performed for elemental analysis (Thermo Fisher Scientific model). The temperature dependence of the magnetization *M(T)* with Zero

Field Cooled (ZFC), Field Cooled (FC) and Field Warmed (FW) protocols under 1 T magnetic field and the field dependence of the magnetization *M(H)* at room temperature (300 K) were measured using a Quantum Design PPMS with VSM option. Electrochemical measurements were carried on Iviumstat potentiostat/galvanostat in a conventional working cell containing SLG on FTO, and Fe_2O_3/SLG on FTO as a working electrode, a Pt wire as counter electrode, and Ag/AgCl as the reference electrode. The electrodes were inserted into a working cell containing 5 mM $K_4Fe(CN)_6$/0.1 M KCl between − 0.8 V and 1.2 V with 100 mV/s of the scan rate.

3 Results and discussion

Figure 1 shows the refined XRD pattern of the as-synthesized Fe_2O_3 nanoparticles. In the figure, the red circle symbol and the thick line represents the observed and calculated patterns, respectively. The thin black line indicates the difference between these patterns. The Bragg positions are also presented. The refinement result shows that there is a good agreement between the observed and the calculated patterns. The structure of Fe_2O_3 was found to be a rhombohedral crystal structure with hexagonal axes (space group; *R-3cH*). The calculated lattice constants are determined as $a = b = 5.032$ Å and $c = 13.739$ Å ($c/a = 2.730$). The result shows that the nanoparticles have α-Fe_2O_3 phase. The crystallite size of the sample was calculated for the strongest Bragg reflection by using Scherrer Formula [57] and found to be 44 nm.

The morphology of the Fe_2O_3 was measured by SEM and presented in Fig. 2. The images show that nanocrystals are agglomerated and the shapes of particles are nearly spherical. The size distribution of particles is also depicted in the inset. The distribution analysis of NPs shows that the mean particle diameter is 128 nm.

SLG, SLG/Fe_2O_3, and the sandwich-type SLG/Fe_2O_3/SLG on FTO have been investigated in bright and dark field mode by optical microscopy (Fig. 3a–f). The dark field microscopy process is useful to see the detail of the materials. Figure 3a–d shows that SLG is located on FTO. After Fe_2O_3 nanoparticles are added on SLG/FTO, they can be easily seen in the images (Fig. 3b–e). In addition, after a second graphene sheet transferred on Fe_2O_3/SLG, two different graphene structures can be distinguished from the edges (Fig. 3c–f).

Raman spectroscopy is widely used to characterize layer number and quality of graphene. The quality of the graphene is determined by the ratio of peak intensities, I_D/I_G. The number of layers of graphene can be derived from the ratio of peak intensities, I_{2D}/I_G. The Raman spectrum as a single layer and the sandwich-type of the graphene obtained in this study are shown in Fig. 4a, b, respectively. The Raman spectrum in Fig. 4a shows the characteristic D band peak at 1368 cm^{-1}, the G peak at 1594 cm^{-1}, the 2D peak at 2712 cm^{-1}. The ratios of peak intensities were calculated as I_D/I_G= 0.62 and I_{2D}/I_G=1.5.

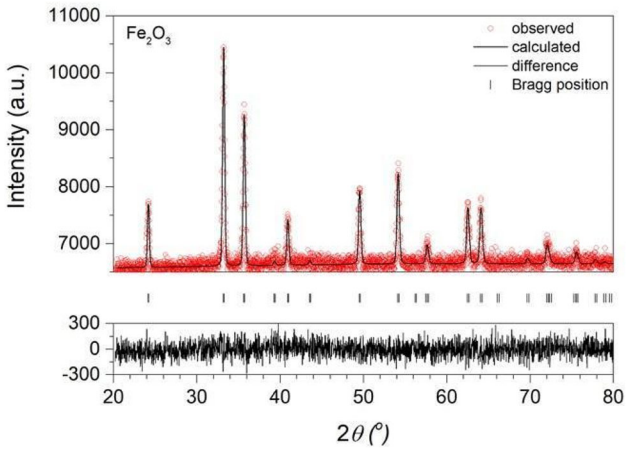

Fig. 1 Rietveld refinement results. Observed (red circles) and calculated (black lines) intensities of XRD patterns of Fe_2O_3 (Color figure online)

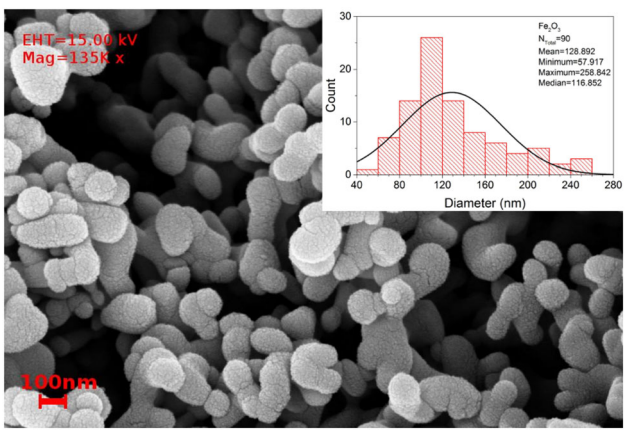

Fig. 2 SEM images of the Fe_2O_3 nanoparticles (histograms of crystallite size diameters obtained from SEM images of the Fe_2O_3 nanoparticles shown in the inset)

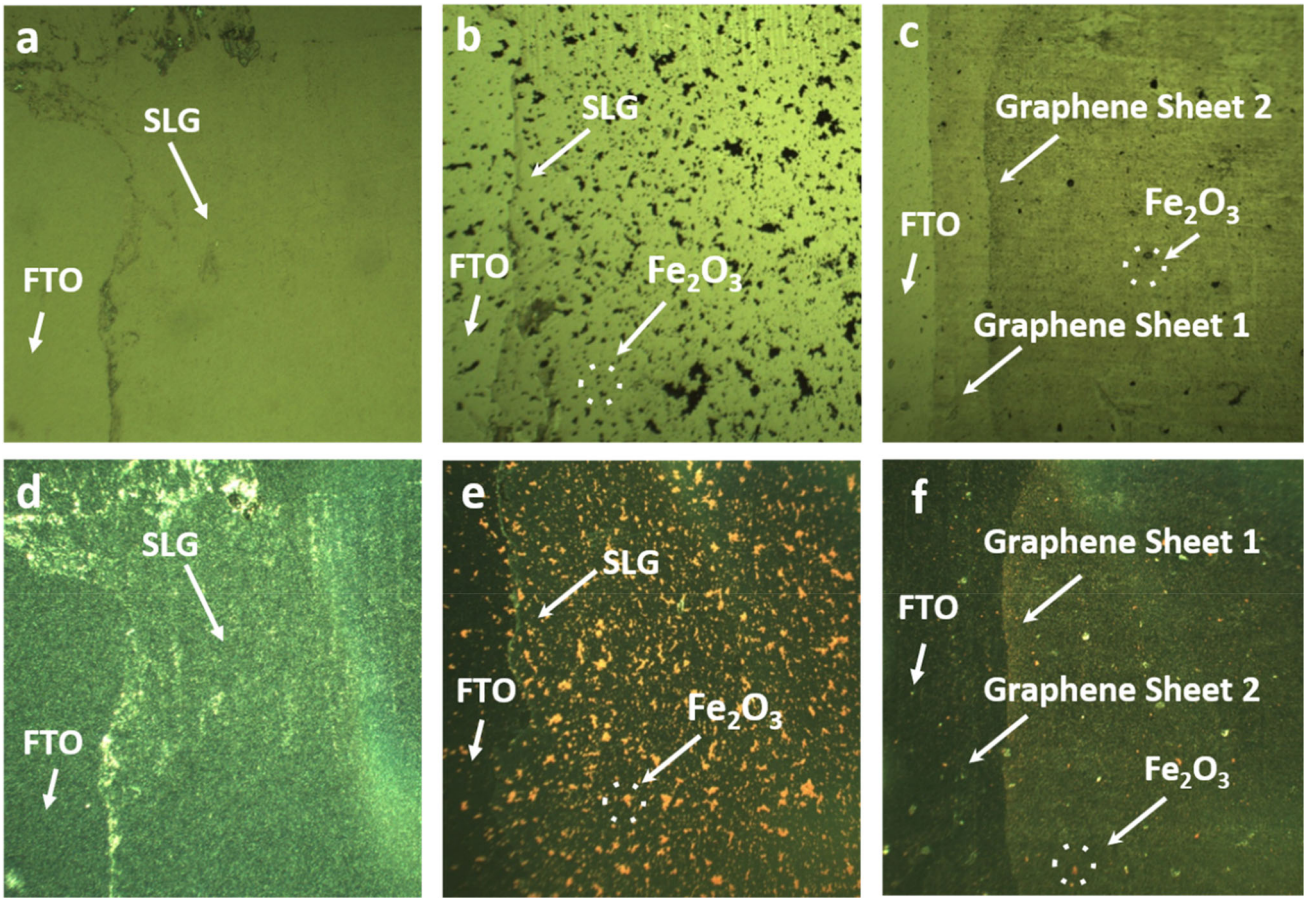

Fig. 3 Microscopic views of **a** SLG on FTO, **b** Fe_2O_3/SLG on FTO, **c** SLG/Fe_2O_3/SLG and the dark field microscope images of **d** SLG on FTO, **e** Fe_2O_3/SLG on FTO, **f** SLG/Fe_2O_3/SLG

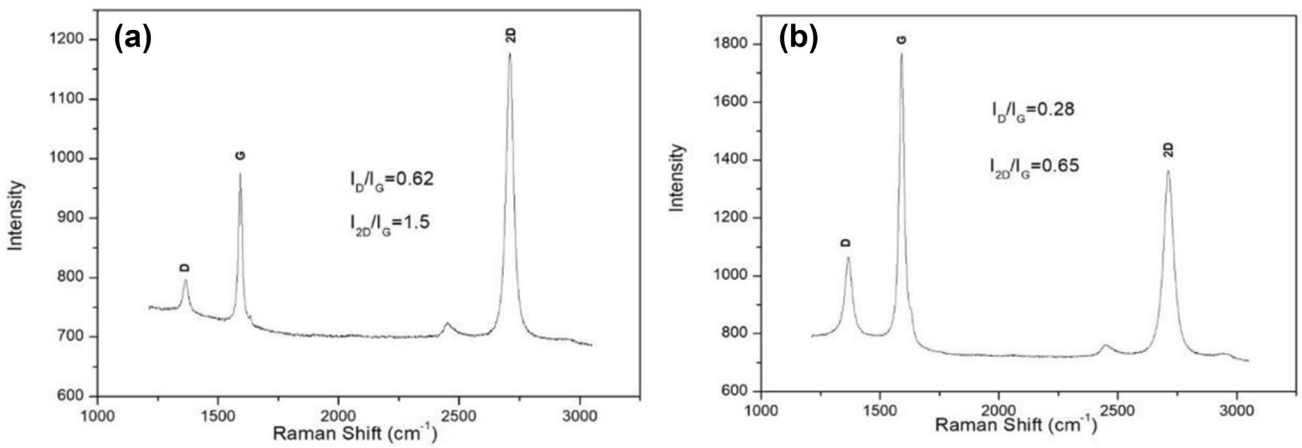

Fig. 4 Raman spectroscopy of **a** Fe_2O_3/SLG on FTO and **b** sandwich-type SLG/ Fe_2O_3/SLG on FTO

General opinion on layer number of graphene is I_{2D}/I_G ratio of > 2, ~ 1, and < 1 is speculated as a single-layer, bilayer, and few-layer graphene, respectively [58, 59]. Consequently, the obtained value indicates single-layer graphene synthesized on FTO. The Raman spectrum in Fig. 4b shows the characteristic D band peak at 1370 cm^{-1}, a G peak at 1589 cm^{-1}, the 2D peak at 2713 cm^{-1}. The ratio of 2D and G peak's intensity is 0.65 proving that sandwich-type (few-layer) graphene is successfully produced in the

study. Furthermore, optical microscopy and SEM analysis also confirm the results of the Raman analysis.

Figure 5 also shows SEM images of FTO (Fig. 5a), SLG (Fig. 5b), Fe_2O_3/SLG (Fig. 5c) and the sandwich-type SLG/Fe_2O_3/SLG (Fig. 5d, e) on FTO. It is possible to distinguish from the images as coated and uncoated (Fig. 5a) with SLG. Furthermore, these images show that the SLG is mostly covered with the Fe_2O_3 nanoparticles. In addition to seeing the differences between bare SLG/FTO surface and Fe_2O_3/SLG/FTO surface. The nanoparticles also appear to be trapped between the graphene layers and are covered by a graphene layer (Fig. 5d, e). Furthermore, in the images, a typically wrinkled, sheet structure of graphene and the presence of very small defects in this graphene layer can be seen.

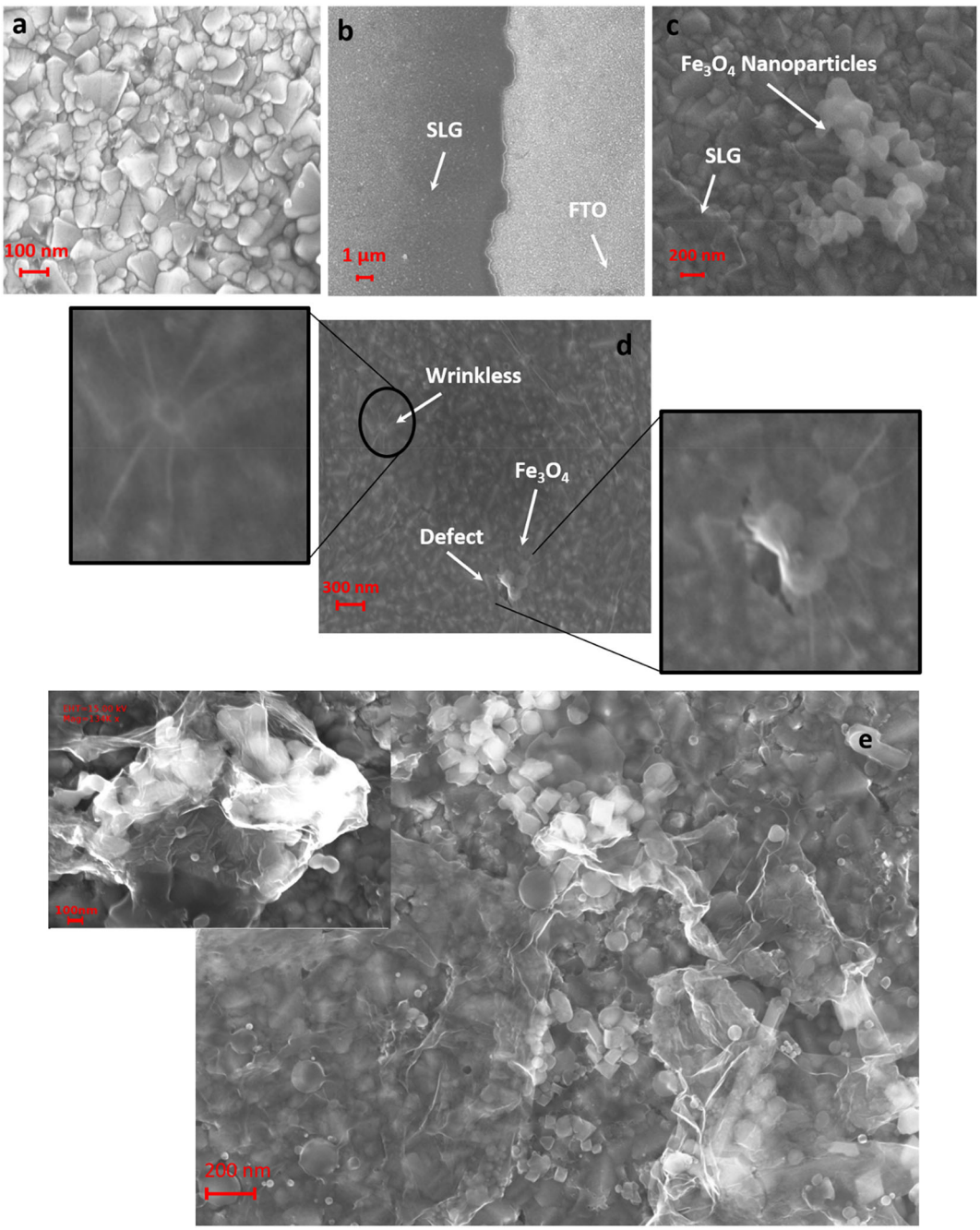

Fig. 5 SEM images of **a** FTO, **b** SLG on FTO, **c** Fe_2O_3/SLG on FTO **d**, **e** sandwich-type SLG/Fe_2O_3/SLG on FTO

EDX spectra of the sandwich-type SLG/Fe_2O_3/SLG on FTO are depicted in Fig. 6. EDX is a standard method for identifying and quantifying elemental compositions. The EDX spectrum confirms the existence of C peaks of graphene, Fe, and O peaks of Fe_2O_3 nanoparticles. In addition, F and Sn peaks of the FTO substrate are also observed. The Si peak arises from the FTO coated glass surface.

Figure 7 represents the XPS of the sandwich-type SLG/Fe_2O_3/SLG on FTO. It shows the presence of various components such as carbon, oxygen, Fe, and FTO at room temperature (Fig. 7a). All the binding energies were corrected using the C 1s reference line at 284.6 eV as a standard. Furthermore, the peaks concerned groups in the C 1s spectra confirm the graphene structure (Fig. 7b). The energies at 286.7 and 289.3 eV can be appointed to C–O, and C=O, respectively. Furthermore, the Fe 2p peaks which are located at approximately 711.2 and 717.0 eV are assigned to Fe $2p_{3/2}$ and Fe $2p_{1/2}$, respectively, indicating that the Fe ions are present in the trivalent form, as depicted in Fig. 7c. The low-intensity peak located around 713.5 eV is a satellite. The O 1s contribution originates from the Fe_2O_3 and FTO (Fig. 7d). Generally, the XPS analysis revealed the presence of Fe_2O_3 nanoparticles and successfully coated the SLG on FTO.

To investigate the magnetic behavior of Fe_2O_3 nanoparticles, the temperature dependence of magnetization was measured at 1 T, which is shown in Fig. 8. In general, Fe_2O_3 has a high Neel temperature of about T_N = 955 K [60]. *M(T)* measurement showed an antiferromagnetic behavior at low temperatures. When the temperature is increased, there is a magnetic phase transition at T = 263 K antiferromagnetic to weak ferromagnetic, which is known as Morin temperature (T_M) or spin-flop transition. This phase transition arises from the two sub-lattices from along to perpendicular to the [111] axis of a rhombohedral structure with hexagonal axes. In the case of spin reorientation, spins are oriented in a direction different from their previous alignment which strongly depends on the value of the applied magnetic field and presents anisotropy in the system. Above T_M temperature, Fe_2O_3 has parasitic ferromagnetism because of spin-canting. Below this temperature, it is antiferromagnetic. Because an equal number of spins arrangement in the two sub-lattices indicates spontaneous antiparallel orientation along the [111] direction of the crystal [61].

Figure 9 shows the magnetic field dependence of the magnetization *M(H)* of Fe_2O_3 measured from $-2T$ to $2T$ magnetic field at room temperature (300 K). As seen in the figure, the Fe_2O_3 particles show no saturation of the magnetization due to the

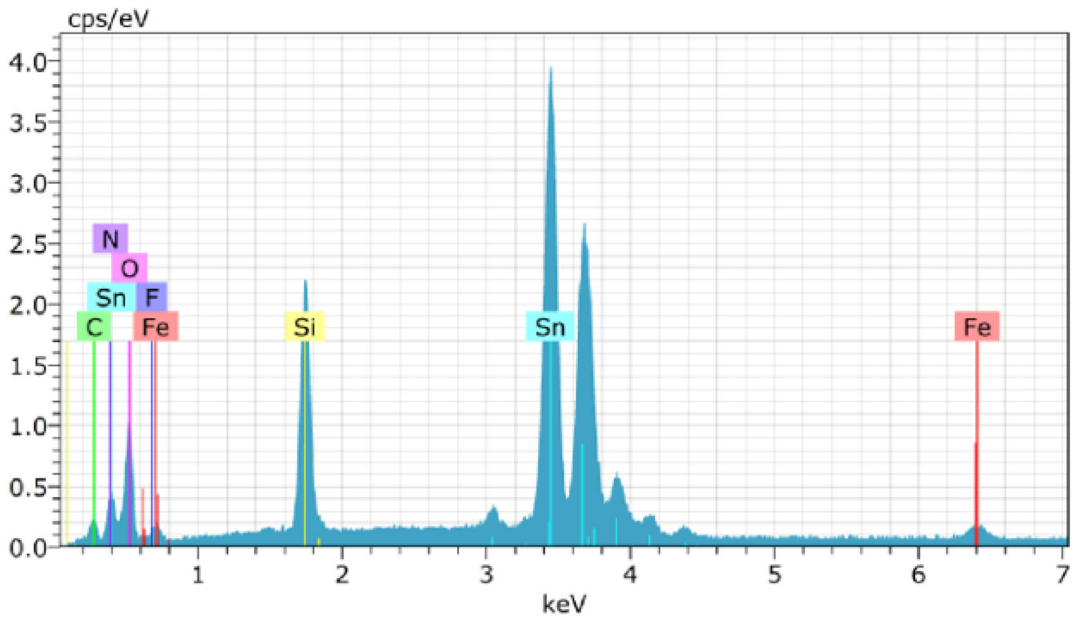

Fig. 6 EDX analysis of the sandwich-type SLG/Fe_2O_3/SLG on FTO. C belongs to graphene and Fe and O belong to Fe_2O_3. F, Sn and Si peaks arise from the FTO coated glass surface

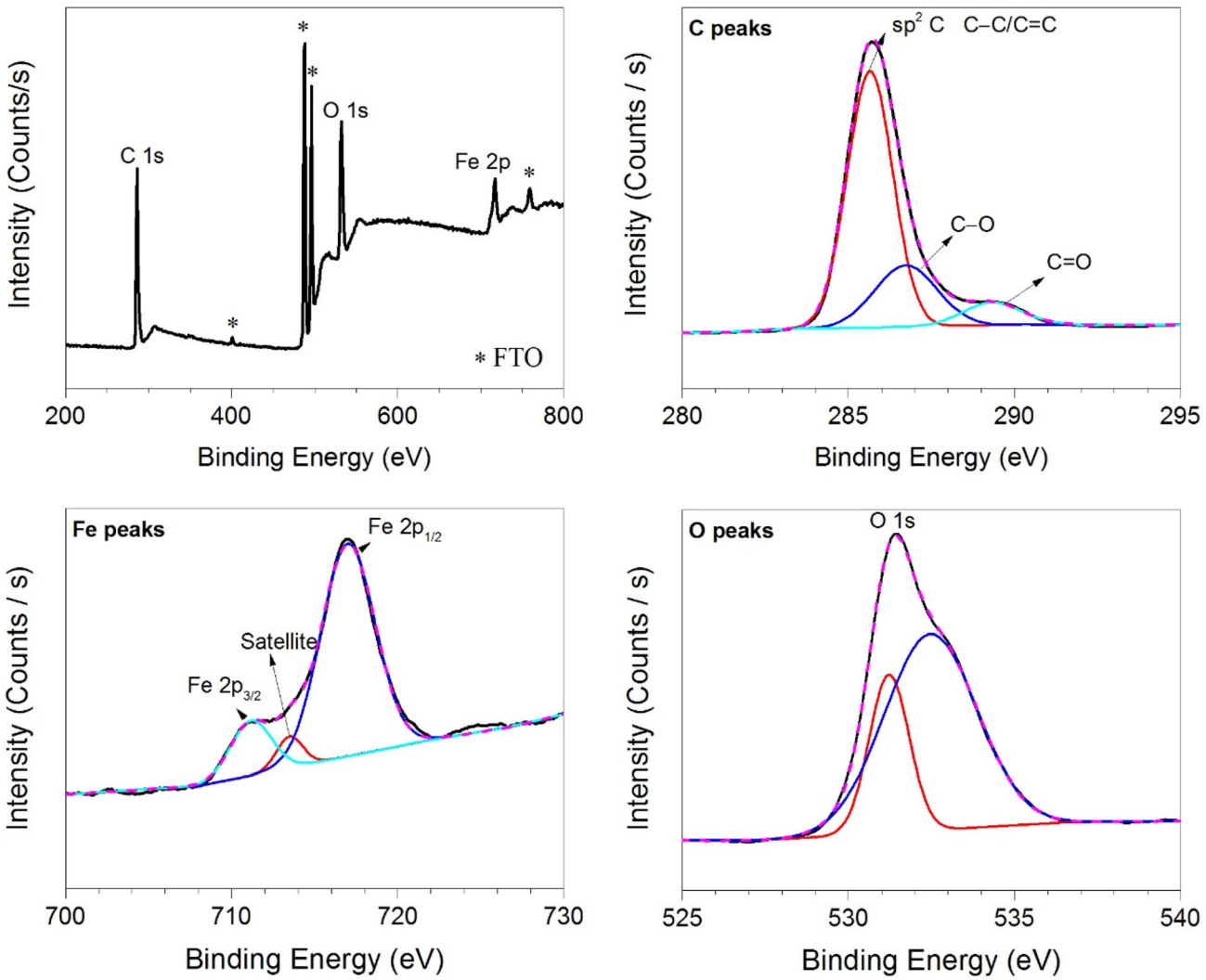

Fig. 7 XPS analysis of SLG/Fe_2O_3/SLG on FTO. Panel **a** shows the broadscan XPS spectra of SLG/ Fe_2O_3/SLG surfaces. Panels **b**, **c** and **d** display C, Fe and O XPS spectra of SLG/Fe_2O_3/SLG surfaces, respectively

presence of the antiferromagnetic phase. By removing the antiferromagnetic contribution on the curve, the saturation value of the ferromagnetic Fe_2O_3 nanoparticles was obtained as 0.31 Am^2/kg. Furthermore, the magnetization curve indicates a weak remanent magnetization of 0.16 Am^2/kg and also coercivity of 0.203 T at room temperature. These results confirm that Fe_2O_3 nanoparticles exhibit rhombohedral α-phase [62].

The electrochemical characterizations of SLG on FTO, and Fe_2O_3/SLG on FTO were investigated using cyclic voltammetry (CV) to understand oxidation-reduction processes of Fe_2O_3 nanoparticles (Fig. 10). When analyzing CV curves of materials, the charge density of Fe_2O_3/SLG/FTO depicts a larger area than SLG/FTO which can be attributed to the active surface area of Fe_2O_3 nanoparticles. In addition, the transferring of Fe_2O_3 nanoparticles on the FTO/SLG, the current density was increased.

4 Conclusion

In summary, to the best of our knowledge, large-area Fe_2O_3/SLG and sandwich-type SLG/Fe_2O_3/SLG composite structure were produced for the first time by CVD and sol–gel process and structure properties were investigated by using XRD, Raman spectroscopy, EDX, XPS, optical microscopy and SEM. α-Fe_2O_3 has a rhombohedral phase and the shapes of

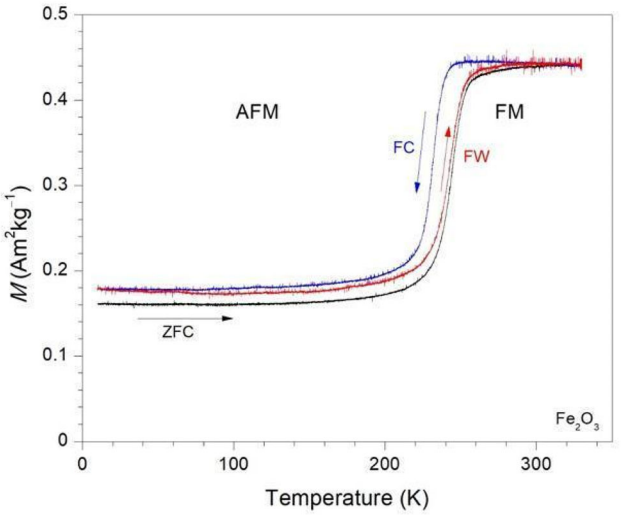

Fig. 8 Magnetization depending on the temperature of Fe_2O_3. Black, red and blue lines with dots indicate ZFC, FW and FC curves, respectively (Color figure online)

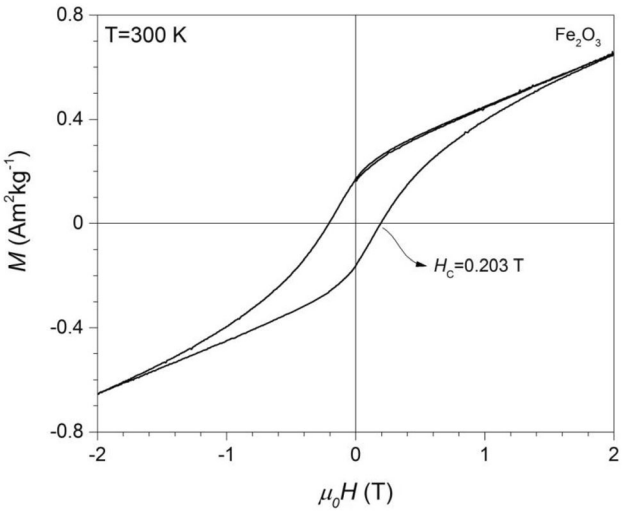

Fig. 9 Hysteresis curves of Fe_2O_3 at 2 T magnetic field at T = 300 K

the particles which contain agglomerates of nanoparticles are spherical with about 128 nm particle diameter. It was observed that the remanent magnetization of Fe_2O_3 nanoparticles is 0.16 Am^2/kg and samples showed almost 0.203 T magnetic coercivity. Furthermore, the structure analysis results indicated that Fe_2O_3/SLG and sandwich-type SLG/Fe_2O_3/SLG composites were successfully obtained. The increase in the charge density of Fe_2O_3/SLG/FTO was clearly observed when compared to SLG/FTO via electrochemical measurements. Moreover, these results demonstrate the feasibility of graphene

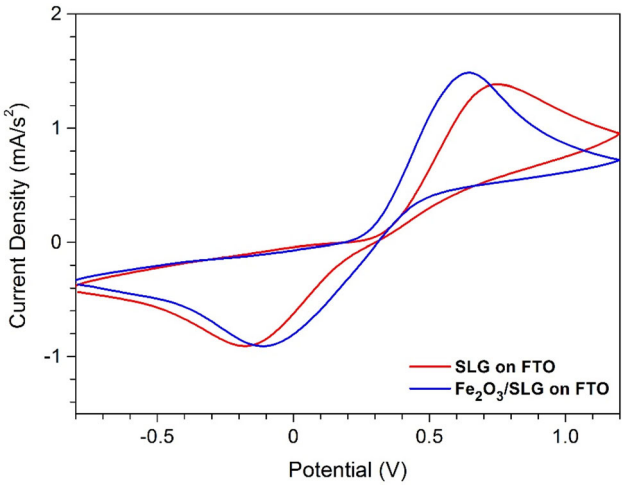

Fig. 10 Cyclic voltammetry analysis of SLG on FTO (red) and Fe_2O_3/SLG on FTO (blue) (Color figure online)

sandwich-type electrodes to eliminate the main stabilization obstacle of magnetic nanoparticles especially for biosensor applications.

Acknowledgements

I thank to Prof. Dr. Metin AK, Dr. Rukiye AYRANCI for CV measurement and Dr. Telem ŞİMŞEK for language editing.

References

1. K.S. Novoselov et al., Two-dimensional atomic crystals. Proc Natl Acad Sci USA **102**, 10451–10453 (2005)
2. R.R. Nair et al., Fine structure constant defines visual transparency of graphene. Science **320**, 1308 (2008)
3. A.K. Geim, Graphene, Status and prospects. Science **324**, 1530–1534 (2009)
4. M.S. Fuhrer, Journal club. A physicist peels back the layers of excitement about graphene. Nature **459**, 1037 (2009)
5. A.H. Castro Neto, F. Guinea, N.M.R. Peres, K.S. Novoselov, A.K. Geim, The electronic properties of graphene. Rev. Mod. Phys. **81**, 109–162 (2009)
6. S. Wu, Q. He, C. Tan, Y. Wang, H. Zhang, Graphene-based electrochemical sensors. Small **9**, 1160–1172 (2013)
7. B. Wang, S. Li, J. Liu, M. Yu, Preparation of nickel nanoparticle/graphene composites for non-enzymatic electrochemical glucose biosensor applications. Mater. Res. Bull. **49**, 521–524 (2014)
8. W. Zhang et al., Multifunctional glucose biosensors from Fe(3)O(4) nanoparticles modified chitosan/graphene nanocomposites. Sci. Rep. **5**, 11129 (2015)

9. L. Li et al., Monolithic Fe_2O_3/graphene hybrid for highly efficient lithium storage and arsenic removal. Carbon **67**, 500–507 (2014)
10. B.-S. Kong, J. Geng, H.-T. Jung, Layer-by-layer assembly of graphene and gold nanoparticles by vacuum filtration and spontaneous reduction of gold ions. Chem. Commun. 2174–2176 (2009)
11. I. Shakir, Z. Ali, D.J. Kang, Layer by layer assembly of gold nanoparticles and graphene via Langmuir Blodgett method for efficient light-harvesting in photocatalytic applications. J. Alloy Compd. **617**, 707–712 (2014)
12. F. Shayeganfar, J. Beheshtiyan, M. Neek-Amal, R. Shahsavari, Electro- and opto-mutable properties of MgO nanoclusters adsorbed on mono- and double-layer graphene. Nanoscale **9**, 4205–4218 (2017)
13. Z. Cai, Y. Ye, X. Wan, J. Liu, S. Yang, Y. Xia, G. Li, Q. He, Morphology-dependent electrochemical sensing properties of iron oxide–graphene oxide nanohybrids for dopamine and uric acid. Nanomaterials **9**, 835 (2019)
14. T. Peng, H. Lv, D. He, M. Pan, S. Mu, Direct transformation of amorphous silicon carbide into graphene under low temperature and ambient pressure. Sci. Rep. **3**, 1148 (2013)
15. T. Peng, Z. Kou, H. Wu, S. Mu, Graphene from amorphous titanium carbide by chlorination under 200 °C and atmospheric pressures. Sci. Rep. **4**, 5494 (2014)
16. K. Ullah, W.-C. Oh, Fabrication of large size graphene and Ti-MWCNTs/large size graphene composites: their photocatalytic properties and potential application. Sci. Rep. **5**, 14242 (2015)
17. T. Soganci, R. Ayranci, E. Harputlu, K. Ocakoglu, M. Acet, M. Farle, C.G. Unlu, M. Ak, An effective biosensor platform design by copper nanoparticles decorated by sputtering on CVD graphene. Sensors Actuators B **273**, 1501–1507 (2018)
18. T. Soganci, R. Ayranci, M. Acet, C.G. Unlu, M. Ak, Designing sandwich-type single-layer graphene decorated by copper nanoparticles for enhanced sensing properties. J. Phys. D: Appl. Phys. **53**, 25 (2020)
19. V. Safarifard, A. Morsali, Facile preparation of nanocubes zinc-based metal-organic framework by an ultrasound-assisted synthesis method; precursor for the fabrication of zinc oxide octahedral nanostructures. Ultrason. Sonochem. **40**, 921–928 (2018)
20. P.A. Asiabi, A. Ramazani, M. Khoobi, M. Amin, M. Shakoori, N.M. Sadegh, R. Farhadi, Regenerated silk fibroin-based dressing modified with carnosine-bentonite nanosheets accelerates healing of second-degree burn wound. Chem. Pap. **74**, 3243–3257 (2020)
21. A. Yaghoubi, A. Ramazani, Anticancer, DOX delivery system based on CNTs: functionalization, targeting and novel technologies. J. Control. Rel. **327**, 198–224 (2020)
22. P. Raizada, A. Sudhaika, P. Singha, A. Hosseini-Bandegharaei, V.K. Guptad, S. Agarwal, Silver-mediated Bi_2O_3 and graphitic carbon nitride nanocomposite as all solid state Z scheme photocatalyst for imidacloprid pesticide abatement from water. Desal. Water Treat. **171**, 344–355 (2019)
23. E. Gholibegloo, A. Karbasi, M. Pourhajibagher, N. Chiniforush, A. Ramazani, T. Akbari, A. Bahador, M. Khoobi, Carnosine-graphene oxide conjugates decorated with hydroxyapatite as promising nanocarrier for ICG loading with enhanced antibacterial effects in photodynamic therapy against *Streptococcus mutans*. J. Photochem. Photobiol. B **181**, 14–22 (2018)
24. M. Razaghi, A. Ramazani, M. Khoobi, T. Mortezazadeh, E.A. Aksoy, T. Tüylü Küçükkılınç, Highly fluorinated graphene oxide nanosheets for anticancer linoleic-curcumin conjugate delivery and T2-weighted magnetic resonance imaging: in vitro and in vivo studies. J. Drug Deliv. Sci. Technol. **60**, 101967 (2020)
25. H. Kamani, S. Nasseri, R. Nabizadeh, M. Khoobi, D.A. Seyed, E. Bazrafshan, A.H. Mahvi, Sonocatalytic oxidation of reactive blue 29 by N-doped TiO_2 from aqueous solution. J. Mazandaran Univ. Med. Sci. **28**(166), 157–169 (2018)
26. F. Moradnia, S.T. Fardood, A. Ramazani, V.K. Gupta, Green synthesis of recyclable $MgFeCrO_4$ spinel nanoparticles for rapid photodegradation of direct black 122 dye. J. Photochem. Photobiol. A **392**, 112433 (2020)
27. S.T. Fardood, R. Forootan, F. Moradnia, Z. Afshari, A. Ramazan, Green synthesis, characterization, and photocatalytic activity of cobalt chromite spinel nanoparticles. Mater. Res. Express **7**(1), 015086 (2020)
28. M. Mohammadi, A. Rezaei, A. Khazaei, S. Xuwei, Z. Huajun, Targeted development of sustainable green catalysts for oxidation of alcohols via tungstate-decorated multifunctional amphiphilic carbon quantum dots. ACS Appl. Mater. Interfaces **11**(36), 33194–33206 (2019)
29. M.S. Yeganeh, A.R. Kazemizadeh, A. Ramazani, P. Eskandari, H.R. Angourani, Plant-mediated synthesis of Cu0.5Zn0.5Fe2O4 nanoparticles using Minidium leavigatum and their applications as an adsorbent for removal of reactive blue 222 dye, Materials Research Express 6 (12), (2020)
30. M. Mohammadi, A. Khazaei, A. Rezaei, Z. Huajun, S. Xuwei, Ionic-Liquid-Modified Carbon Quantum Dots as a Support for the Immobilization of Tungstate Ions (WO42–) Heterogeneous Nanocatalysts for the Oxidation of Alcohols in Water. ACS Sustainable Chemistry & Engineering **7**(5), 5283–5291 (2019)
31. B.E. Azar, A. Ramazani, S.T. Fardood, A. Morsali, Green synthesis and characterization of ZnAl2O4@ZnO nanocomposite and its environmental applications in rapid dye degradation. Optik **208**, 164129 (2020)

32. X.-W. Yan, M. Joharian, M. Naghiloo, R. Rasuli, R. Hu, M.-L. Morsali, A., Metal–organic framework derived porous 2D semiconductor C/ZnO nanocomposite with the high electrical conductivity. Mater. Lett. **252**, 325–328 (2019)
33. N.-N. Zhang, F. Bigdeli, Q. Miao, M.-L. Hu, A. Morsali, Ultrasonic-assisted synthesis, characterization and DNA binding studies of Ru(II) complexes with the chelating N-donor ligand and preparing of RuO2 nanoparticles by the easy method of calcination. J. Organomet. Chem. **878**, 11–18 (2018)
34. E.S. Mehr, M. Sorbiun, A. Ramazani, S.T. Fardood, Plant-mediated synthesis of zinc oxide and copper oxide nanoparticles by using ferulago angulata (schlecht) boiss extract and comparison of their photocatalytic degradation of Rhodamine B (RhB) under visible light irradiation. J. Mater. Sci.: Mater. Electron. **29**(2), 1333–1340 (2018)
35. A.M.K. Pasha, M. Hosseini, A. Fakhri, V.K. Gupta, S. Agarwal, Investigation of photocatalytic process for iron disulfide-bismuth oxide nanocomposites by using response surface methodology: Structural and antibacterial properties. J. Mol. Liq. **289**, 110950 (2019)
36. T. Mortezazadeh, E. Gholibegloo, N. Riyahi Alam, S. Haghgoo, A.E. Musa, M. Khoobi, Glucosamine Conjugated Gadolinium (III) Oxide Nanoparticles as a Novel Targeted Contrast Agent for Cancer Diagnosis in MRI. Journal of Biomedical Physics and Engineering **10**(1), 25–38 (2020)
37. S.M. Pormazar, M.H. Ehrampoush, M.T. Ghaneian, M. Khoobi, P. Talebi, A. Dalvand, Application of amine-functioned Fe3O4 nanoparticles with HPEI for effective humic acid removal from aqueous solution: Modeling and optimization. Korean J. Chem. Eng. **37**(1), 93–104 (2020)
38. A. Ansari, S. Vahedi, O. Tavakoli, M. Khoobi, M.A. Faramarzi, Novel Fe3O4/hydroxyapatite/β-cyclodextrin nanocomposite adsorbent: Synthesis and application in heavy metal removal from aqueous solution. Appl. Organomet. Chem. **33**(1), e4634 (2019)
39. J.-J. Xue, F. Bigdeli, J.-P. Liu, M.-L. Hu, A. Morsali, Ultrasonic-assisted synthesis and DNA interaction studies of two new Ru complexes; RuO_2 nanoparticles preparation. Nanomedicine **13**(21), 2691–2708 (2018)
40. K. Atrak, A. Ramazani, S.T. Fardood, Eco-friendly synthesis of $Mg_{0.5}Ni_{0.5}Al_xFe_{2-x}O_4$ magnetic nanoparticles and study of their photocatalytic activity for degradation of direct blue 129 dye. J. Photochem. Photobiol. A **382**, 111942 (2019)
41. F. Zarekarizi, S. Beheshti, A. Morsali, Solid-state preparation of mixed metal-oxides nanostructure from anionic metal-organic framework via cation exchange process. Inorg. Chem. Commun. **97**, 144–148 (2018)
42. S.T. Fardood, F. Moradnia, A. Ramazani, Green synthesis and characterisation of $ZnMn_2O_4$ nanoparticles for photocatalytic degradation of Congo red dye and kinetic study. Micro Nano Lett. **14**(9), 986–991 (2019)
43. F. Parsa, M. Massomeh Ghorbanloo, M.Y. Masoomi, A. Morsali, P.C. Junk, J. Wang, Ultrasound-assisted synthesis and characterization of a new metal-organic framework based on azobenzene-4,4-dicarboxylic acid: precursor for the fabrication of Co_3O_4 nano-particles. Ultrason. Sonochem. **45**, 197–203 (2018)
44. F. Moradnia, A. Ali Ramazani, S.T. Fardood, F. Gouranlou, A novel green synthesis and characterization of tetragonal-spinel $MgMn_2O_4$ nanoparticles by tragacanth gel and studies of its photocatalytic activity for degradation of reactive blue 21 dye under visible light. Mater. Res. Express **6**(7), 075057 (2019)
45. P. Hayati, S. Suárez-García, A. Gutierrez, E. Şahin, D.R. Molina, A. Morsali, A.R. Rezvani, Sonochemical synthesis of two novel Pb(II) 2D metal coordination polymer complexes: new precursor for facile fabrication of lead(II) oxide/bromide micro-nanostructures. Ultrason. Sonochem. **42**, 310–319 (2018)
46. A. Jordan et al., Presentation of a new magnetic field therapy system for the treatment of human solid tumors with magnetic fluid hyperthermia. J Magn Magn Mater **225**, 118–126 (2001)
47. M.H. Falk, R.D. Issels, Hyperthermia in oncology. Int. J. Hyperther. **17**, 1–18 (2001)
48. I. Hilger et al., Thermal ablation of tumors using magnetic nanoparticles: an in vivo feasibility study. Invest. Radiol. **37**, 580–586 (2002)
49. I. Hilger et al., Magnetic nanoparticles for selective heating of magnetically labelled cells in culture: preliminary investigation. Nanotechnology **15**, 1027–1032 (2004)
50. C.Y. Cummings, M.J. Bonné, K.J. Edler, M. Helton, A. Mckee, F. Marken, Direct reversible voltammetry and electrocatalysis with surface-stabilized Fe_2O_3 redox states. Electrochem. Commun. **10**, 1773–1776 (2008)
51. R. Ahmad, M.A. Ahn, Y.A. Hahn, Highly Sensitive, Nonenzymatic sensor based on Fe_2O_3 nanoparticle coated ZnO nanorods for electrochemical detection of nitrite. Adv. Mater. Interfaces **4**, 1700491 (2017)
52. G.K. Larsen, W. Farr, S.E.H. Murph, Multifunctional Fe_2O_3–Au nanoparticles with different shapes: enhanced catalysis, photothermal effects, and magnetic recyclability. J. Phys. Chem. C **120**, 15162–15172 (2016)
53. M.A. Zayed, M.A. Ahmed, N.G. Imam, D.H.El Sherbiny, Preparation and structure characterization of hematite/magnetite ferro-fluid nanocomposites for hyperthermia purposes. J. Mol. Liq. **222**, 895–905 (2016)
54. H. Quan, B. Cheng, Y. Xiao, S. Lei, One-pot synthesis of α-Fe_2O_3 nanoplates-reduced graphene oxide composites for

supercapacitor application. Chem. Eng. J. **286**, 165–173 (2016)
55. J.L. Gunjakar, A.M. More, K.V. Gurav, C.D. Lokhande, Chemical synthesis of spinel nickel ferrite ($NiFe_2O_4$) nanosheets. Appl. Surf. Sci. **254**, 5844–5848 (2008)
56. T. Soganci, R. Ayranci, M. Acet, C.G. Unlu, M. Ak, Enhanced sensing properties of CuNP islands decorated in large area sandwich type single layer graphene. J. Phys. D **53**, 25 (2020)
57. B.D. Cullity, *Elements of X-Ray Diffraction* (Addison-Wesley, Philadelphia, 1978)
58. A.C. Ferrari, Raman spectroscopy of graphene and graphite: disorder, electron–phonon coupling, doping and nonadiabatic effects. Solid State Commun. **143**, 47–57 (2007)
59. Y. Hao et al., Probing layer number and stacking order of few-layer graphene by Raman spectroscopy. Small **6**, 195–200 (2010)
60. C. Frandsen, S. Morup, Spin rotation in alpha-Fe_2O_3 nanoparticles by interparticle interactions. Phys. Rev. Lett. **94**, 027202 (2005)
61. S.A. McEnroe et al., Magnetic exchange bias of more than 1 T in a natural mineral intergrowth. Nat. Nanotechnol. **2**, 631–634 (2007)
62. E. Kendir, A. Tekgül, Ş Küçük, Yaltkaya, Structural, optical and magnetic properties of α-Fe_2O_3-SiO_2 and Dy_2O_3-SiO_2 composites produced by a Facile method. J. Electr. Mater. **49**, 798–806 (2020)